A 3D bioprinted nano-laponite hydrogel construct promotes osteogenesis by activating PI3K/AKT signaling pathway

Sheng Miao [a,1], Jinru Zhou [b,1], Bin Liu [c,1], Xing Lei [d], Taoran Wang [a], Xiaotian Hao [e], Pengzhen Cheng [a], Hao Wu [a], Yue Song [f], Guoxian Pei [a,**], Long Bi [a,*]

[a] Department of Orthopedics, Xijing Hospital, Air Force Medical University, Xi'an, 710032, China
[b] Department of Radiology, Luoyang Central Hospital Affiliated to Zhengzhou University, Luoyang, 471000, China
[c] Department of Orthopedics, General Hospital of Northern Theater Command, Shenyang, 110015, China
[d] Department of Orthopedics, Linyi People's Hospital, Linyi, 276002, China
[e] College of Life Sciences, Northwest University, Xi'an, 710069, China
[f] Department of Orthopedics, Fourth Medical Center of PLA General Hospital, Beijing, 100048, China

ARTICLE INFO

ABSTRACT

Development of nano-laponite as bioinks based on cell-loaded hydrogels has recently attracted significant attention for promoting bone defect repairs and regeneration. However, the underlying mechanisms of the positive function of laponite in hydrogel was not fully explored. In this study, the effect of 3D bioprinted nano-laponite hydrogel construct on bone regeneration and the potential mechanism was explored *in vitro* and *in vivo*. *In vitro* analyses showed that the 3D construct protected encapsulated cells from shear stresses during bioprinting, promoted cell growth and cell spreading, and BMSCs at a density of 10^7/mL exhibited an optimal osteogenesis potential. Osteogenic differentiation and ectopic bone formation of BMSCs encapsulated inside the 3D construct were explored by determination of calcium deposition and x-ray, micro-CT analysis, respectively. RNA sequencing revealed that activation of PI3K/AKT signaling pathway of BMSCs inside the laponite hydrogel significantly upregulated expression of osteogenic related proteins. Expression of osteogenic proteins was significantly downregulated when the PI3K/AKT pathway was inhibited. The 3D bioprinted nano-laponite hydrogel construct exhibited a superior ability for bone regeneration in rat bones with defects compared with groups without laponite as shown by micro-CT and histological examination, while the osteogenesis activity was weakened by applications of a PI3K inhibitor. In summary, the 3D bioprinted nano-laponite hydrogel construct promoted bone osteogenesis by promoting cell proliferation, differentiation through activation of the PI3K/AKT signaling pathway.

1. Introduction

Conventional grafting methods used for the reconstruction of bone defects caused by trauma, infection, and tumors are associated with various limitations (supply and morbidity associated with autograft harvest, minor immunogenic rejection, and risk of disease transmission with allografts) [1,2]. Advances in three-dimensional (3D) bioprinting have significantly revolutionized bone regeneration techniques [3,4]. Bioprinting is an advanced manufacturing method used to design and fabricate complex biological structures, because the integration of designed structural and biological complexities through conventional fabrication methods is challenging [5]. João Mano et al. had confirmed that proper porosity by 3D printing could improve the efficiency of cell seeding on the scaffold and induce a more uniform distribution [6]. This ensures the multifunctionality of printing osteogenic precursor cell-incorporated bioinks (hydrogels) layer-by-layer and controls spatial resolution as well as cell distribution to mimic the native architectures of bone tissues. Bioinks are key components of the bioprint technology [2].

This technology also includes printable materials, seed cells, and biological factors that enhance the biological activities of cells while preserving shape fidelity during free-form deposition as extruded filaments [7]. However, the bioprinting of tough hydrogels involves additional complexities, including performance-complex crosslinking or incorporation of reinforcing mechanisms during printing and pre/post-printing [4,5].

Nanocomposites with exceptional properties play a key role in biomedical nanotechnology applications [8,9]. The incorporation of laponite can significantly enhance the rheological capacities and mechanical properties of hydrogels [10]. Laponite is a relatively safe FDA-approved material that can be used as a carrier of cell growth factors [5]. The degradation products of laponite, including magnesium ions, silicic acid, and lithium ions, exhibit biological activities such as the promotion of osteogenic differentiation of mesenchymal stem cells [11]. Our research team has previously developed a biomimetic and functional hydrogel scaffold incorporating laponite through 3D bioprinting [12]. *In vitro* and *in vivo* analyses revealed that laponite can improve the osteogenic differentiation of bone mesenchymal stem cells (BMSCs) in the absence of additional osteoinductive factors, which vary with different cell seeding densities. However, the mechanism underlying the effects of laponite on osteogenic differentiation has not been fully elucidated [11, 13].

BMSCs are multipotent progenitor cells localized in the stromal compartment of the bone marrow. These cells exhibited osteogenic differentiation potential [14]. During cultivation in medium, the cells at low densities exhibited poor proliferative capacity, whereas at high densities, they exhibited low viability [15,16]. However, it has not been determined whether the density of BMSCs inside 3D bioprinted hydrogels influences their biological functions.

In this study, the effect of a bioprinted laponite hydrogel construct loaded with BMSCs on osteogenesis was evaluated, and the potential mechanisms were explored *in vitro* and *in vivo*. The effects of different cell densities on the printability, mechanical properties, swelling, and hydration characteristics of the bioprinted hydrogel construct were investigated. Furthermore, *in vitro* biocompatibility and osteogenic properties of the constructs were evaluated. Ectopic bone formation was investigated in a rat muscle pouch model. Furthermore, possible mechanisms were explored by evaluating upregulated osteogenesis-associated genes using RNA sequencing and KEGG pathway analyses. Finally, a rat cranial bone defect model was established, and the regulation of the specific pathways through which this bioprinted laponite hydrogel construct induced osteogenesis was determined.

2. Experimental

2.1. Fabrication of bioprinted hydrogel constructs and analysis of their characteristics

2.1.1. BMSC isolation and identification

BMSCs were extracted from the long bone marrow of 2-week-old Sprague-Dawley (SD) rats [17] (provided by the Experimental Animal Center of the Fourth Military Medical University) and cultured in MEM alpha modification (α-MEM) (HyClone, Cat No: SH30265.01) medium supplemented with 10% fetal bovine serum (FBS) (Gibco, Cat No: 10270-106) and 1% penicillin-streptomycin solution (Solarbio, Cat No: P1400). Cells were incubated in an incubator (Thermo Fisher Scientific, USA) with 5% CO_2 humidified atmosphere at 37 °C. The medium was replaced every two days to remove non-adherent cells. BMSCs were obtained at 80–90% colony confluence and subcultured using trypsin (HyClone, Cat No: SH30042.01). Third-generation BMSCs were used in subsequent experiments.

Flow cytometric analysis was performed to determine the presence of MSC-positive (CD29 and CD90) and MSC-negative (CD11b/c, CD34, and CD45) surface markers using the appropriate antibodies (Biolegend, USA).

2.1.2. Preparation of bioink

Hydrogels were prepared as previously described [12]. A blended hydrogel comprising 10% gelatin (48722-500G-F, Sigma-Aldrich, USA), 1% alginate (A0682-100G, Sigma-Aldrich, USA), and 2% laponite (BYK-Chemie GmbH, Germany) was prepared using deionized water at 30 °C. BMSCs were gently mixed with the hydrogel at different cell densities (0, 1×10^5/mL, 1×10^6/mL, 1×10^7/mL and 1×10^8/mL BMSCs indicates T0, T5, T6, T7 and T8, respectively) to obtain various bioinks.

2.1.3. 3D bioprinting process

All constructs were printed using a bioprinter (Particle Cloud, Xi'an, China). Bioinks with different cell densities were respectively loaded into an extruder cartridge, with a temperature at 30 °C. The STL files were loaded into the bioprinter program. The parameters for the bioprinter were set as follows: moving speed, 50 mm/s; flow rate, 12.72 mL/h, and nozzle height, 300 μm. Constructs of the complex were printed onto homothermal metal plates (at room temperature), as shown in Fig. 1a. Cylinders (8 mm in diameter and 5 mm in height) were fabricated for the mechanical and swelling tests, whereas cuboids with dimensions of 15 mm × 15 mm × 2 mm were constructed for the other experiments. The bioprinted constructs were immersed in 2% w/v $CaCl_2$ solution to allow cross-linking with calcium for 10 min and then gently washed three times with phosphate-buffered saline (PBS). The constructs were transferred to a complete medium and cultured in an incubator under 5% CO_2. Morphologies of the cells inside the bioprinted constructs were explored on days 1 and 7 using an optical microscope (BX53, Olympus, Japan).

2.1.4. X-ray diffraction (XRD) and Fourier transform infrared (FTIR) spectroscopy

The structures of the biocomposite and each raw material were determined using infrared spectroscopy and diffraction patterns. The FTIR measurements were performed using a Nicolet iS5 infrared spectrometer (Thermo Corporation, USA). X-ray diffraction (XRD) data were obtained using a D8-Advance X-ray diffractometer (Bruker Corporation, Germany) equipped with nickel-filtered Cu-Kα radiation at 40 kV/30 mA. The patterns were collected at a scan speed of 0.02°/s at 2 theta angle of 10°–70°. Before the FTIR and XRD results were measured, the biocomposite was ground into a powder.

2.1.5. Mechanical testing

Compression tests were performed using a universal material tester (MTS Systems, Minneapolis, MN, USA) to evaluate the mechanical properties of the bioprinted cylinders with different cell densities. Samples from each group were analyzed at a compression speed of 2 mm/min and a preliminary load of 0.3 N. Compressive modulus was calculated using the following equation:

$$E = \frac{F \times L}{S \times \Delta L}$$

where F is the compressive force, L is the original height of the samples, S is the area of the upper compression surface of the samples, and ΔL is the relative deformation of the samples under the force. All experiments were performed in triplicates at room temperature.

2.1.6. Swelling tests

Hydration of the bioprinted cylinders with different cell densities was determined by immersing six samples from each group in PBS for 12 h, and each wet weight was recorded after careful removal of excess PBS on the surface using a filter paper. The samples were then completely lyophilized and their dry weights were recorded. The swelling ratio was determined using the following equation: *Swelling ratio* $= \frac{W_{wet} - W_{dry}}{W_{dry}}$, whereas the hydration degree was calculated as follows: *Hydration degree* $= \frac{W_{wet} - W_{dry}}{W_{wet}} \times 100\%$.
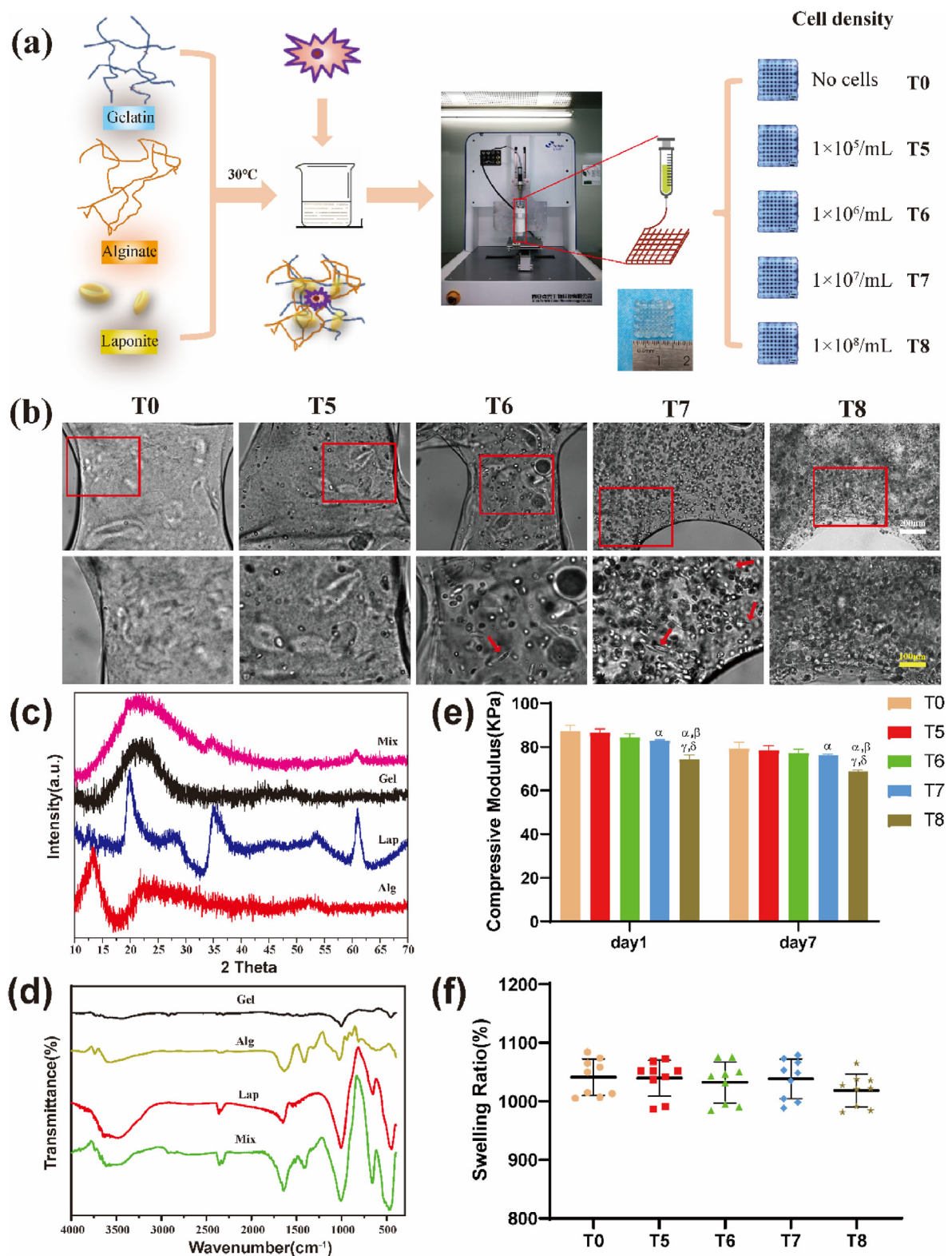
Fig. 1. Preparation and characterization of 3D printed composite hydrogel biological scaffolds. (a) 3D printing preparation process of the biological scaffolds. Hydrogels were assigned to five groups according to densities of loaded cells. (b) Cells were evenly distributed in the hydrogel scaffold, with some of the cells being stretched in a spindle shape (red arrows) as observed under an optical microscope. Scale bars: white 200 μm, yellow 100 μm. (c) XRD patterns and (d) FTIR spectra of Gel, Alg, Lap and the Mixture after bioprinting. (e) Compression modulus of cell-loaded hydrogels on the day 1 and day 7 after preparation. (f) Swelling ratios of each group indicated that cell density had no significant effect on hydration performance of the hydrogels with high water contents. $^{\alpha}P<0.05$ vs T0; $^{\beta}P<0.05$ vs T5; $^{\gamma}P<0.05$ vs T6; $^{\delta}P<0.05$ vs T7. (For interpretation of the references to colour in this figure legend, the reader is referred to the Web version of this article.)

2.2. Biocompatibility and osteogenic property analyses

2.2.1. Live/dead cell assay

The viability of cells inside the hydrogels was explored using a live/dead assay (Dojindo Laboratories, Japan) on days 3, 7, and 14. Bioprinted cuboid samples from each group were washed three times with PBS and then transferred to a staining solution (α-MEM supplemented with 10 mM calcein-AM and 10 mM propidium iodide (PI)). After incubation for 3 h in a CO_2 atmosphere, the live cells were stained in green by calcein-AM ($\lambda_{ex}/\lambda_{em}$ = 490 nm/515 nm), while the dead cells were stained in red by PI ($\lambda_{ex}/\lambda_{em}$ = 530 nm/580 nm). The staining solution was washed with PBS and the samples were observed under a laser confocal scanning microscope (Nikon A1R, Japan).

2.2.2. Cell microfilament staining

The live/dead cell assay indicated that T7 was the optimal density for cell survival; thus, the cytoskeletal structure of the cells in this group was explored on day 7 of incubation. The samples were gently washed three times with PBS, fixed in 4% paraformaldehyde (Solarbio, China), and treated with 0.5% Triton X-100 (Sigma, USA) to rupture the cytomembrane, followed by washing with PBS. The samples were stained with phalloidin (Cytoskeleton Inc., USA) for 30 min and DAPI (Solarbio, China) for 5 min. Imaging was performed using a laser confocal scanning microscope.

2.2.3. Alizarin red S staining

Calcium deposits were evaluated on days 7, 14, and 21 after bioprinting. Samples from each group were fixed in 4% paraformaldehyde for 30 min and gently washed three times with PBS, followed by overnight dehydration in a solution of 30% sucrose and 10% gum arabic (Sigma, USA). Frozen sections were prepared, and serial sections were washed with PBS for 30 s to remove the Opti-mum Cutting Temperature compound and stained with Alizarin Red S (Solarbio, China) according to the manufacturer's instructions. Imaging was performed using an optical microscope (BX53, Olympus). The mineralization capacities of the samples were determined by calculating the area covered by the mineralized nodules.

2.2.4. Scanning electron microscopy (SEM) and energy-dispersive X-ray spectroscopy (EDS) analysis

SEM (Hitachi, Japan) equipped with an EDS spectrometer (Bruker, Germany) was used to analyze the morphology and composition of the mineralized nodules generated in the hydrogel construct. Specimens were harvested on day 21 after bioprinting and gently rinsed three times with deionized water to remove Ca^{2+} dissolved on the surface, followed by dehydration with graded ethanol. The samples were then dried under vacuum. Gold spraying was performed on the surface and examined using SEM. Calcium nodules were captured and magnified using an acceleration voltage of 15 kV. The elements in each sample were qualitatively and semi-quantitatively analyzed using an X-ray energy spectrum analyzer.

2.2.5. Alkaline phosphatase (ALP) activity assay

Crosslinks for three samples in each group were untied using sodium citrate on days 7, 14, and 21, and cells in the bioprinted hydrogel were collected. ALP activity was determined using an ALP assay kit (Beyotime, China), and total protein levels were evaluated using a BCA kit (Beyotime, China). ALP activity was normalized to the total protein concentration of the samples.

2.2.6. Expression analysis of osteogenesis-associated genes

Total RNA was extracted from each sample by using a universal RNA extraction kit (Takara, Xi'an, China). cDNA was synthesized using 500 ng total RNA and 2 μL PrimeScript RT Master Mix (Takara, Xi'an, China) according to the manufacturer's instructions. Quantitative real-time reverse-transcriptase PCR was performed using TB Green Premix Ex Taq II (Takara, Xi'an, China) on a CFX96 Real-Time PCR Detection System (Bio-Rad Laboratories Inc., USA). The primers used in this study are listed in Table S1. Glyceraldehyde-3-phosphate dehydrogenase (GAPDH) was used as the control.

2.3. Ectopic bone formation analysis

After preparation, the bioprinted cuboids were placed in complete medium to maintain cell viability, and transplantation was performed *in vivo* on the same day to simulate the fate of cells mixed with the hydrogel *in vivo* as much as possible.

2.3.1. Surgical procedure

Animal experiments and procedures were approved by the Experimental Animal Ethics Committee of Fourth Military Medical University. Forty-five Sprague-Dawley rats (male, approximately 250 g) were purchased from the Experimental Animal Center of the Fourth Military Medical University and used for ectopic bone formation analysis. Anesthesia was induced by the intraperitoneal administration of pentobarbital sodium (40 mg/kg). The posterior gluteal area was then shaved and disinfected using iodine disinfectant. Subsequently, one bioprinted cuboid was bilaterally implanted into the posterior gluteal muscle punch of nine rats from each group. The wound was gently sutured after implantation. Three rats from each group were euthanized 2, 4, and 8 weeks after implantation to harvest the implants.

2.3.2. X-ray and micro-computed tomography (micro-CT) imaging

Whole hind legs of rats were dissected at predefined time points and perfused with 4% paraformaldehyde for X-ray imaging. The samples were then gently isolated from the muscle punches. The samples were scanned using a micro-CT system (YXLON, Germany), and 3D images were reconstructed using VG Studio MAX software (Volume Graphics, Heidelberg, Germany) for bone formation analysis. The voltage and the current were 80 kV and 55.6 μA, respectively, and the image pixel size was 17 μm. The bone volume to total volume (BV/TV) ratio was determined.

2.3.3. EDS of samples

An energy-dispersive X-ray spectrometer was used to analyze the elemental compositions of each sample to explore the mineralization of the ectopically embedded samples following a previously described method [8].

2.3.4. Tissue immunofluorescence staining

The levels of Runx2, osterix, OCN, and Col-1α proteins in each sample were evaluated by immunofluorescence at week 4 post-operation. Deparaffinized sections were rehydrated with deionized water, retrieved using sodium citrate buffer, and blocked with 10% non-specific binding goat serum. Further, sections were incubated with primary antibodies against Runx2 (Abcam, ab23981, 1:200), osterix (Abcam, ab22552, 1:200), OCN (Abcam, ab13420, 1:200), and Col-1α (Abcam, ab34710, 1:500) overnight at 4 °C. The samples were further incubated with fluorescent dye-conjugated secondary antibodies and counterstained with DAPI. Images were obtained using a laser confocal scanning microscope (Nikon A1R, Tokyo, Japan).

2.3.5. Masson's trichrome staining

Excised tissues that had been stored in a fixative solution were embedded in paraffin. The samples were decalcified in 10% ethylenediaminetetraacetic acid (EDTA) for 2 weeks. Embedded tissues were sectioned to obtain 5 μm slices and stained using Masson's trichrome after deparaffinization for ossification analysis.

2.3.6. Sirius red staining

A Sirius red stain kit (Solarbio, China) was used to determine the composition of newly formed fibers in the material tissues. Sections were

deparaffinized using toluene and stained according to the manufacturer's instructions. Collagen fiber imaging, mainly collagen I and III, was performed under an optical microscope (BX53; Olympus, Tokyo, Japan) using polarized light.

2.4. Investigation of mechanisms of different activities

2.4.1. RNA sequencing and bioinformatics analyses

Transcriptome sequencing was performed to explore the mechanism of osteogenesis promotion by laponite. Total RNA was isolated from BMSCs obtained from the bioprinted laponite hydrogels (Hyd_Lap) using TRIzol reagent (Invitrogen, Carlsbad, USA) after two weeks of cultivation, according to the manufacturer's instructions. Cells in bioprinted hydrogels without laponite (Hyd) were used as the controls. RNA sequencing was performed at LC Biotech (Zhejiang, China) to determine the expression profiles of the mRNAs in the different groups. mRNAs with a fold change of log2 >1 or < -1 and $p < 0.05$ were considered differentially expressed. A volcano map was generated to show the number of differentially expressed mRNAs, including the upregulated and downregulated mRNAs. Gene ontology (GO) analysis was used for functional annotation of genes. The overall trend in gene expression is presented as a heatmap. The Kyoto Encyclopedia of Genes and Genomes (KEGG) was used to analyze the signaling pathways in which differentially expressed genes were enriched. The top 20 significantly enriched signaling pathways (p <0.05) were visualized using a scatter bubble chart. The PI3K/AKT pathway, highlighted by the red box, is highly enriched. Bioinformatic analyses were performed using online LC tools (https://www.omicstudio.cn/tool).

2.4.2. Western blot analysis

BMSCs were cultured in bioprinted hydrogels with or without laponite to explore the role of the PI3K/AKT signaling pathway. Cells cultivated in normal culture plates were used as the blank group. Total protein was extracted from the cells using RIPA Lysis Buffer (Beyotime, China), according to the manufacturer's instructions. Proteins were separated using 10% SDS-PAGE and transferred to 0.22 μm polyvinylidene fluoride (PVDF) membranes (Millipore, Germany). PVDF membranes were blocked with 5% (w/v) non-fat dried skim milk TBST solution, then incubated with primary antibodies against p-PI3K (CST4228, 1:1000, USA), PI3K (CST4292, 1:1000, USA), *p*-AKT (CST4060, 1:1000, USA), AKT (CST4691, 1:1000, USA), *p*-mTOR (Santa293133, 1:500, USA), and mTOR (Santa517464, 1:500, USA) overnight at 4 °C. The cells were then incubated with a corresponding horseradish peroxidase (HRP)-conjugated secondary antibody (Proteintech, SA00001-1 and SA00001-2, 1:2000, China) at room temperature for 2 h. ECL Plus reagent (Millipore, Germany) was used to detect the protein bands. LY294002 (MCE, USA) was used to suppress PI3K phosphorylation to verify the role of PI3K/AKT signaling. Protein expression was evaluated using the following primary antibodies: Runx2 (Abcam, ab23981, 1:1000, UK), Col-1α (Abcam, ab34710, 1:1000, UK), and GAPDH (Elabscience, E-AB-20032, 1:1000, China). GAPDH was used as a loading control.

2.4.3. Alizarin red s staining

Staining was performed as described in section 2.2.3.

2.5. Critical-sized cranial defect rat models

2.5.1. Surgical procedure

Bioprinted hydrogel materials were prepared, cultured in complete medium, and implanted on the same day. Fifteen male SD rats (12 weeks old, approximately 300 g) were used to establish critical-sized cranial defect rat models and were assigned to five groups. Anesthesia was induced by intraperitoneal administration of pentobarbital sodium (40 mg/kg), and circular defects (d = 8 mm) were created in the rat skulls. A bioprinted hydrogel without laponite was implanted into the defect to establish the Hyd group, whereas a bioprinted hydrogel with laponite was implanted into Hyd_Lap rats. Laponite hydrogels were implanted, followed by intraperitoneal administration of LY294002 twice weekly for 4 weeks in rats in the Hyd_Lap + LY294002 group. To confirm the role of BMSCs in promoting bone regeneration in the hydrogel, laponite hydrogels without BMSCs were implanted in Hyd_Lap (no BMSCs) as a control. The blank group consisted of rats without implantation in the defect. Samples (n = 3) from each group were radiographically and histologically analyzed 8 weeks post-surgery.

2.5.2. Micro-CT analysis

Rats were euthanized on week 8, and their skulls were harvested. Skull tissues were fixed in 4% neutral paraformaldehyde for 72 h and transferred to 70% ethanol. The skulls were examined using micro-computed tomography. The voltage and the current were 80 kV and 55.6 μA respectively, and the image pixel size was 10 μm 3D images were reconstructed to explore the formation of new bone. Various parameters, including bone volume/total volume (BV/TV), trabecular thickness (TbTh), and trabecular number (TbN) were determined in the region of interest (ROI) with a diameter of 8 mm.

2.5.3. Van Gieson staining

The undecalcified specimens were then embedded in methyl methacrylate. The samples were sectioned, stained using the Van Gieson method, and observed under an optical microscope.

2.5.4 Hematoxylin and eosin staining. At the corresponding time points, the hearts, livers, spleens, lungs, and kidneys of the rats were obtained. After fixing in 4% neutral paraformaldehyde for 72 h, the visceral tissues were dehydrated using gradient alcohol, embedded in paraffin, and sectioned using conventional procedures. The sections were then stained with hematoxylin-eosin after deparaffinization and observed under an optical microscope.

2.6. Statistical analysis

Quantitative data are expressed as mean ± SD for n = 3. Differences between multiple or two groups were analyzed using a one-way analysis of variance or Student's t-test, respectively. SPSS 19.0 (SPSS Inc., Chicago, IL, USA) or GraphPad Prism 8 (La Jolla, CA, USA) software was used for statistical analyses. The significance level was set at p < 0.05.

3. Results

3.1. Hydrogel construct synthesis and characterization

3.1.1. Cell identification

The presence of BMSCs was confirmed by identifying the expression levels of two MSC-positive (CD29 and CD90) and three MSC-negative (CD34, CD45, and CD11b) surface markers of BMSCs (Figure S1).

3.1.2. Fabrication of biological scaffolds

Constructs were prepared and assigned to five groups (T0, T5, T6, T7, and T8) based on the densities of the added BMSCs (Fig. 1a). Optical microscopy revealed high viability and spreading of BMSCs in the frame of bioprinted hydrogel constructs from days 1 to 7 for the T5, T6, T7, and T8 groups. By contrast, no cells were observed in the T0 group. The cells were intensively distributed with increasing cell density. Notably, some cells began to spread in a spindle shape on day 7 (Fig. 1b).

3.1.3. X-ray diffraction (XRD) and Fourier transform infrared (FTIR) spectroscopy

The diffraction peaks of the raw materials exhibited unique characteristics. Fig. 1c shows that the peaks of laponite were mostly located at 2 theta 20°, 35°, and 61°, while gelatin at 2 theta 22° and alginate at 2 theta 13°, respectively, indicating that these raw ingredients were satisfactory. The diffraction peaks of the biocomposite were primarily

located at 2 theta 22°, 35°, and 61°, reflecting the presence of each raw material in the composite. The FTIR spectrum (Fig. 1d) of the composite showed peaks at 2943 cm^{-1}, 1418 cm^{-1}, and 1013 cm^{-1}, which correspond to the characteristic absorption peaks of gelatin, alginate, and laponite, respectively, indicating that the original ingredients did not vary after bioprinting.

3.1.4. Mechanical properties

The strain–stress relationship curve showed that the stress increased with increasing strain (Figure S2). Notably, the addition of BMSCs at different densities caused a mild decrease in compressive modulus. Hydrogel cylinders in the T8 group exhibited a significantly lower compressive modulus on days 1 and 7 ($p < 0.05$), whereas the decrease in compressive modulus for all other cell-loaded groups was not significantly different from that of the T0 group ($p > 0.05$; Fig. 1e).

3.1.5. Hydration analysis

The results showed no significant differences in the swelling ratios among the samples from the different hydrogel groups ($p > 0.05$). Notably, the swelling ratios for all groups were less than 1100% (Fig. 1f). The hydrate formation rate of the hydrogels was approximately 91.2% and the analysis did not show significant differences among the groups ($p > 0.05$; Figure S3).

3.2. Biocompatibility and osteogenic property of hydrogels

3.2.1. Viability and survival status of BMSCs inside hydrogels

Live cells were stained with green fluorescence, whereas dead cells were stained with red fluorescence. The cell survival status and gradual proliferation inside the bioprinted hydrogels of each group at days 3, 7, and 14 are presented in Fig. 2a. During the printed scaffolds being cross-linked and washed, the laponite on the surface could form a complex with Ca and PBS, which would adsorb the red dye PI due to electrostatic effect [18,19]. Therefore, when the scaffolds were stained, some lumps of red may appear in addition to the scattered red dots of dead cells. The cells in each group initially maintained a high activity level in the hydrogel. With the extension of the culture time, the number of cells, including live cells and dead cells, gradually increased (Fig. 2b). Cell viability in live/dead images was quantified using ImageJ software (Fig. 2c). The findings showed that the number of viable cells in the T8 group was less than 90% on day 3 and decreased to less than 85% on day 14. The survival rates in the other groups were >90% on day 14. After culturing the hydrogels for 7 days *in vitro*, BMSCs were attached and spread evenly inside the hydrogels, as shown by the polygonal and slender actin filaments (red) around the nucleus (blue) (Fig. 2d). This indicates that the bioprinted construct can provide suitable 3D conditions to mimic the *in vivo* environment for BMSC adhesion and migration.

3.2.2. Osteogenic differentiation and mineralization

Alizarin red S staining was performed to explore mineralization. Red nodules representing the formation of mineralized matrices were observed in the experimental groups (T5, T6, T7 and T8), whereas the control group (T0) did not exhibit mineralized matrices throughout the culture period (Fig. 3a). Quantitative analysis showed that the level of mineralized matrices in the T7 group was higher than that in the other groups, indicating that BMSCs at 1×10^7/mL density had an optimal osteogenic differentiation performance (Fig. 3b). SEM and EDS analyses were performed to explore the elemental composition of the nodules formed in the hydrogel after culturing the BMSCs for 21 days. The distribution of calcium and phosphorus and spectrograms of the constituent elements in the selected area are presented in Fig. 3c. The levels of different elements in the newly formed nodules, including carbon, hydrogen, oxygen, calcium, phosphorus, and silicon, were similar to those in bone. The ratio of calcium and phosphorus (1.4 ± 0.17) was not significantly different relative to that of hydroxyapatite (approximately 1.67).

3.2.3. Expression levels of osteogenic genes

ALP activity in BMSCs from each group increased from day 7 to 21. ALP activity of BMSCs in the T7 group (83.40 ± 6.75) was significantly higher than that in the other three groups on day 14 ($p < 0.05$; Fig. 3d). In the detection of osteogenic genes, to confirm the promotion effect of laponite on BMSCs in the hydrogel, a cells/hydrogel compound without laponite was set as a control group. The expression levels of osteogenesis-associated genes in the hydrogel containing laponite were higher than those in the control group (hydrogel without laponite; $p < 0.05$, Fig. 3e–i), clearly indicating that laponite promoted the osteogenic differentiation of BMSCs in the hydrogel. Although the expression levels of the early marker gene (Runx2) and its downstream gene (osterix) were slightly suppressed on day 14 compared to day 7, the T7 group with a cell density of 10^7/mL had the highest expression level compared to the other groups ($p < 0.05$). Other osteogenesis-associated genes (ALP, OCN, and Col1a) were not significantly expressed on day 7; however, they showed a trend similar to that of Runx2 and osterix on day 14.

3.3. Ectopic osteogenesis in muscle pouch

3.3.1. X-ray and EDS spectrum analysis

The results showed that images of implants in the T0 group were almost uncaptured at all time points, whereas the images of implants in groups T5, T6, T7, and T8 exhibited varying degrees of mineralization with increasing time (Fig. 4a). Hydrogel constructs were gently isolated from the separated hind legs (Fig. 4b). Implanted constructs become increasingly integrated with the surrounding tissues over time. The texture of the material became hard and a sense of sand was felt upon scratching the inside with a scalpel during isolation. EDS was performed to analyze the components and verify bone formation in the implanted constructs. A uniform distribution of calcium and phosphorus was observed in the presence of representative bone elements. The ratio of calcium to phosphorus was approximately 1.57 ± 0.23, similar to the ratio of hydroxyapatite (Fig. 4c).

3.3.2. Micro-CT analysis

Microstructures and bone masses were determined by micro-CT scanning to quantify the amount of mineralized bone inside the bioprinted constructs which had been implanted in muscle pouches. New bone (silver white) and soft tissues (yellow) were segmented using a threshold value of 2000 HU (Fig. 4d). The BV fraction was calculated as the new bone volume divided by the total material tissue (BV/TV) (Fig. 4e). The four cell-loaded groups exhibited significantly better bone formation than the T0 group, with almost no mineralized bone formation in the T0 group, which was consistent with the X-ray results (Fig. 4a). The BV/TV results showed that the T5 group exhibited the lowest amount of mineralized bone formation at week 2 compared to the four cell-loaded groups, whereas the T8 (12.20 ± 0.82%) and T7 (11.55 ± 1.16%) groups exhibited better bone formation relative to the T6 (7.59 ± 1.08%) group ($p < 0.05$). The T7 group showed the best bone formation at weeks 4 and 8, with bone formation levels of 18.39 ± 0.84% and 21.46 ± 1.03%, respectively.

3.3.3. Immunofluorescence staining for osteogenic-related proteins

Immunofluorescence staining was performed four weeks after transplantation to explore the expression levels of osteogenic-related proteins (Runx2, osterix, OCN, and Col-1a) in the samples. Very low or no protein fluorescence signal was detected in the T0 (no cell loading) group, whereas the other four groups showed different degrees of immunofluorescence signals (Fig. 5a). Staining results revealed that the immunofluorescence signal intensities of Runx2, Osterix, and OCN in the T6, T7, and T8 groups were not significantly different ($p > 0.05$); however, they were stronger than those of the T5 group. The fluorescence intensity of Col-1a in T7 was stronger than that in the other groups ($p < 0.05$).
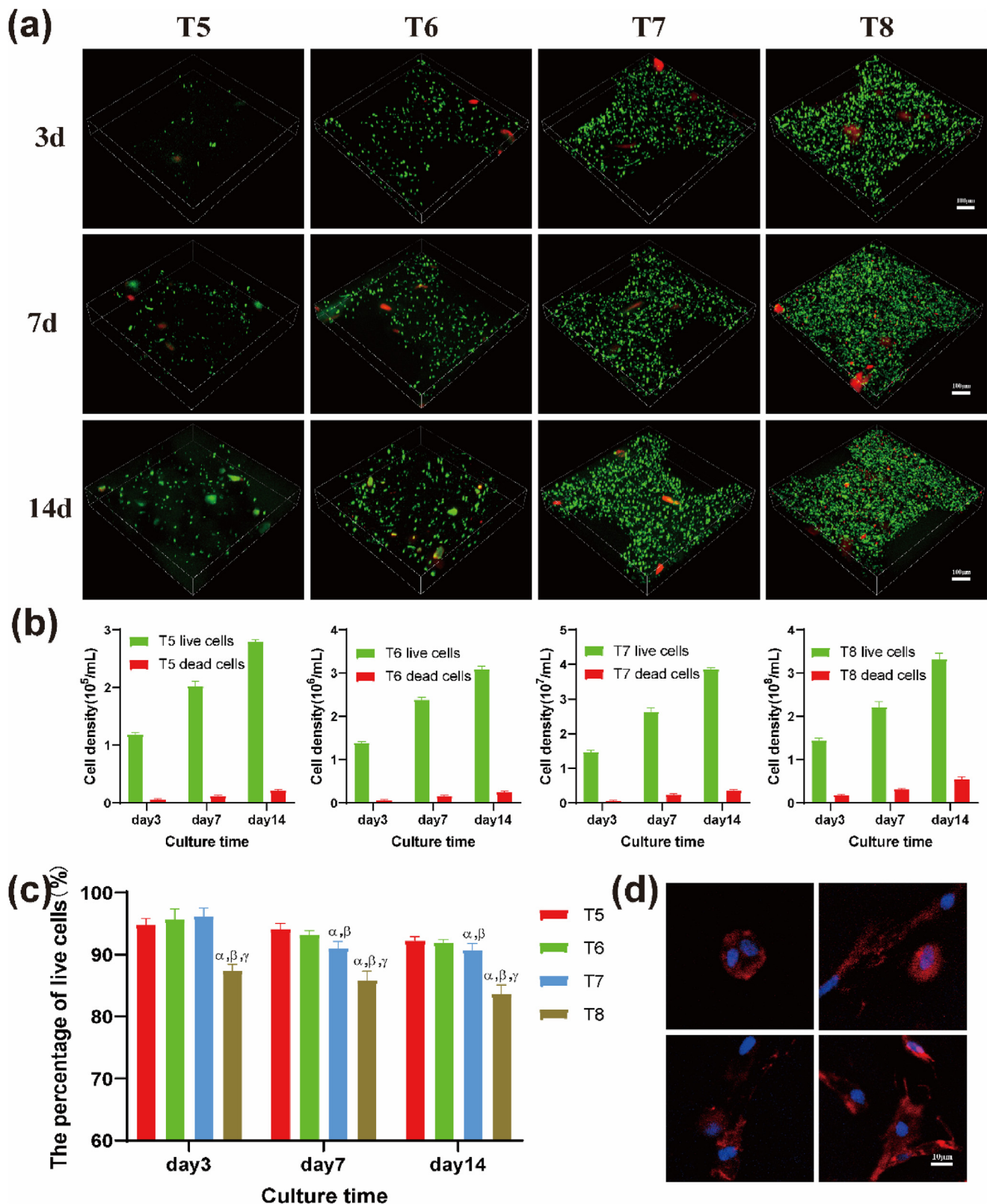
Fig. 2. Survival, proliferation rate and growth status of BMSCs 3D cultured in hydrogel scaffolds at different cell densities. (a) Live/dead stain images of BMSCs in 3D printed hydrogel scaffolds at different cell densities after 3, 7, and 14 days of culture *in vitro* (green represents live cells, red represents dead cells). Scale bar: 100 μm. Statistics of the proliferation (b) and survival rate (c) of BMSCs in each group of hydrogel scaffolds after culturing for 3, 7, and 14 days. (d) Images of F-actin staining of BMSCs cytoskeleton in the T7 group on the day 7 of culture showing cell division and contact with adjacent cells under a randomly selected field of view. Scale bar: 10 μm $^{\alpha}$p<0.05 vs T5; $^{\beta}$p<0.05 vs T6; $^{\gamma}$p<0.05 vs T7. (For interpretation of the references to colour in this figure legend, the reader is referred to the Web version of this article.)
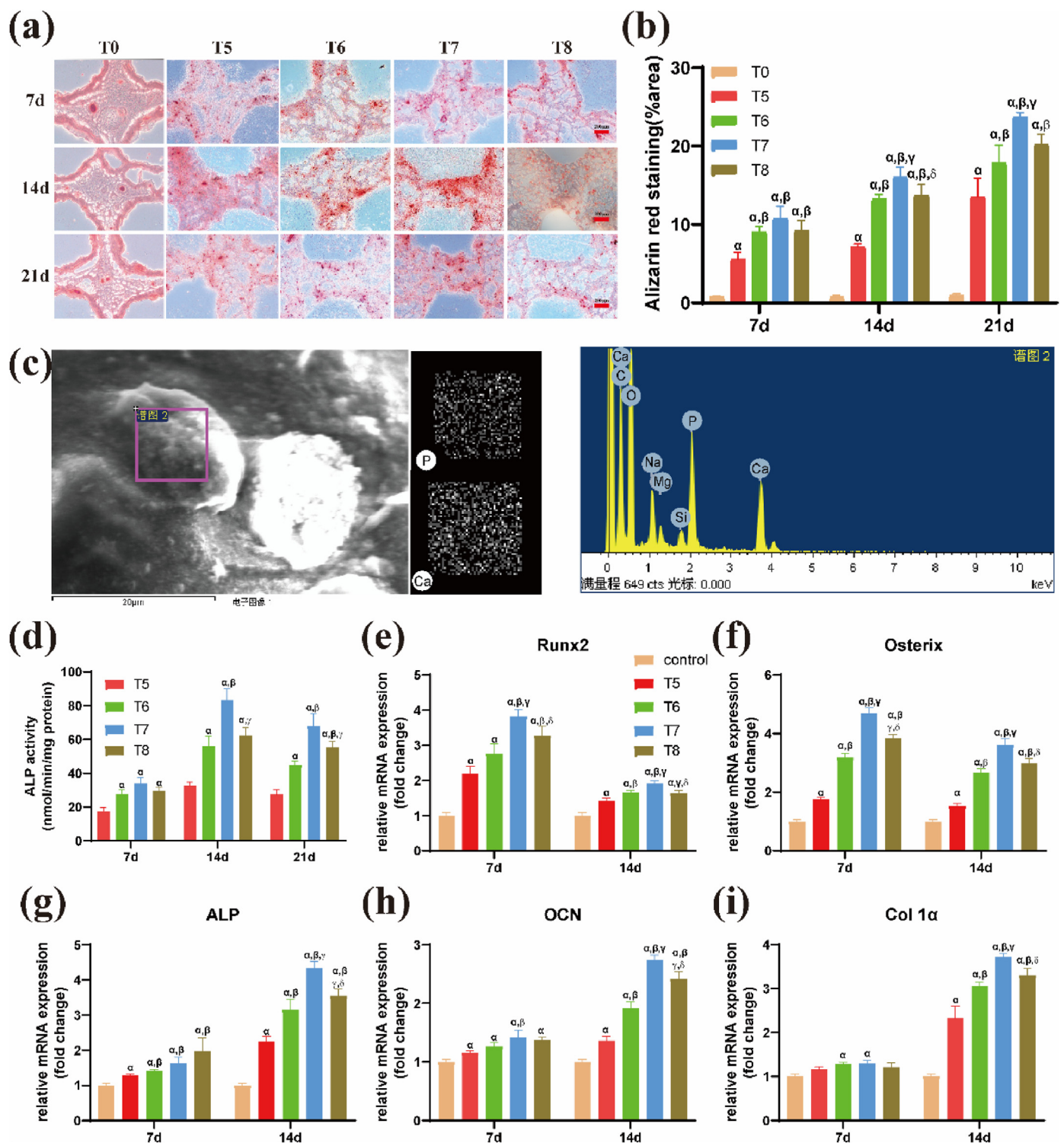
Fig. 3. Effects of density of BMSCs on osteogenic differentiation and mineralization of 3D bio-printed hydrogel scaffolds. (a) Mineralization of hydrogel scaffolds with different densities of BMSCs *in vitro* for day 7, 14, and 21 as shown by alizarin red staining. (b) Quantitation of mineralization levels of hydrogels. Scale bar: 200 μm $^{\alpha}$p<0.05 vs T0; $^{\beta}$p<0.05 vs T5; $^{\gamma}$p<0.05 vs T6; $^{\delta}$p<0.05 vs T7. (c) Elemental composition of mineralized nodules as determined by Energy Dispersive X-ray Spectroscopy (EDS). Scanning electron micrograph of mineralized nodules, elemental distribution of P and Ca elements, and the spectrum of various elemental compositions are shown. (d) Quantitative assays of Alkaline phosphatase (ALP) activity of encapsulated BMSCs in hydrogel scaffolds after culturing for 7, 14, and 21 days. $^{\alpha}$p<0.05 vs T5; $^{\beta}$p<0.05 vs T6; $^{\gamma}$p<0.05 vs T7. Relative gene expression levels of osteogenic markers (e) Runt-related transcription factor 2 (Runx2), (f) Osterix, (g) ALP, (h) osteocalcin (OCN) and (i) type I collagen (Col-1) of BMSCs after day 7 and day14 culture in the hydrogels. $^{\alpha}$p<0.05 vs control; $^{\beta}$p<0.05 vs T5; $^{\gamma}$p<0.05 vs T6; $^{\delta}$p<0.05 vs T7. (For interpretation of the references to colour in this figure legend, the reader is referred to the Web version of this article.)
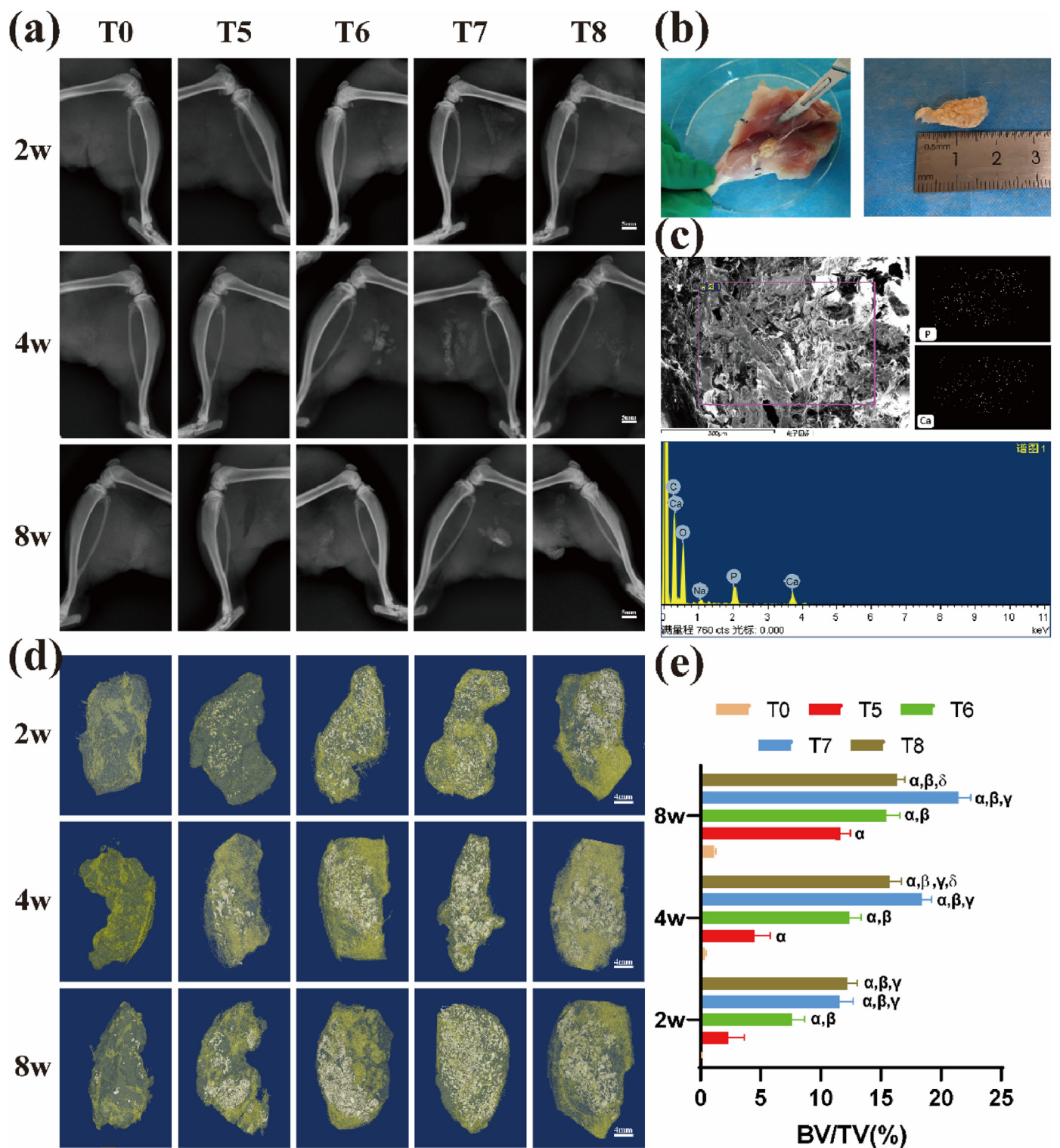
Fig. 4. Mineralized bone formation after ectopic implantation of 3D bio-printed hydrogel scaffolds with different densities of BMSCs. (a) X-ray images of rats' posterior gluteus muscle pouches implanted with biological scaffolds at week 2, 4 and 8. Scale bar: 5 mm. (b) A schematic illustration of isolation of mineralized biological scaffolds from rat posterior gluteal muscle pouches. (c) EDS energy spectrum analysis of mineralized scaffolds. Scanning electron micrographs of mineralized nodules, distribution of P and Ca elements, and spectrums of various elemental compositions are shown. (d) Micro-CT imaging of biological scaffolds with different densities of BMSCs implanted in rat muscle pouches after 2, 4, and 8 weeks (silver color represents mineralized bone, yellow represents fibrous soft tissue) and (e) the corresponding bone volume fraction. Scale bar: 4 mm $^\alpha$p<0.05 vs T0; $^\beta$p<0.05 vs T5; $^\gamma$p<0.05 vs T6; $^\delta$p<0.05 vs T7. (For interpretation of the references to colour in this figure legend, the reader is referred to the Web version of this article.)
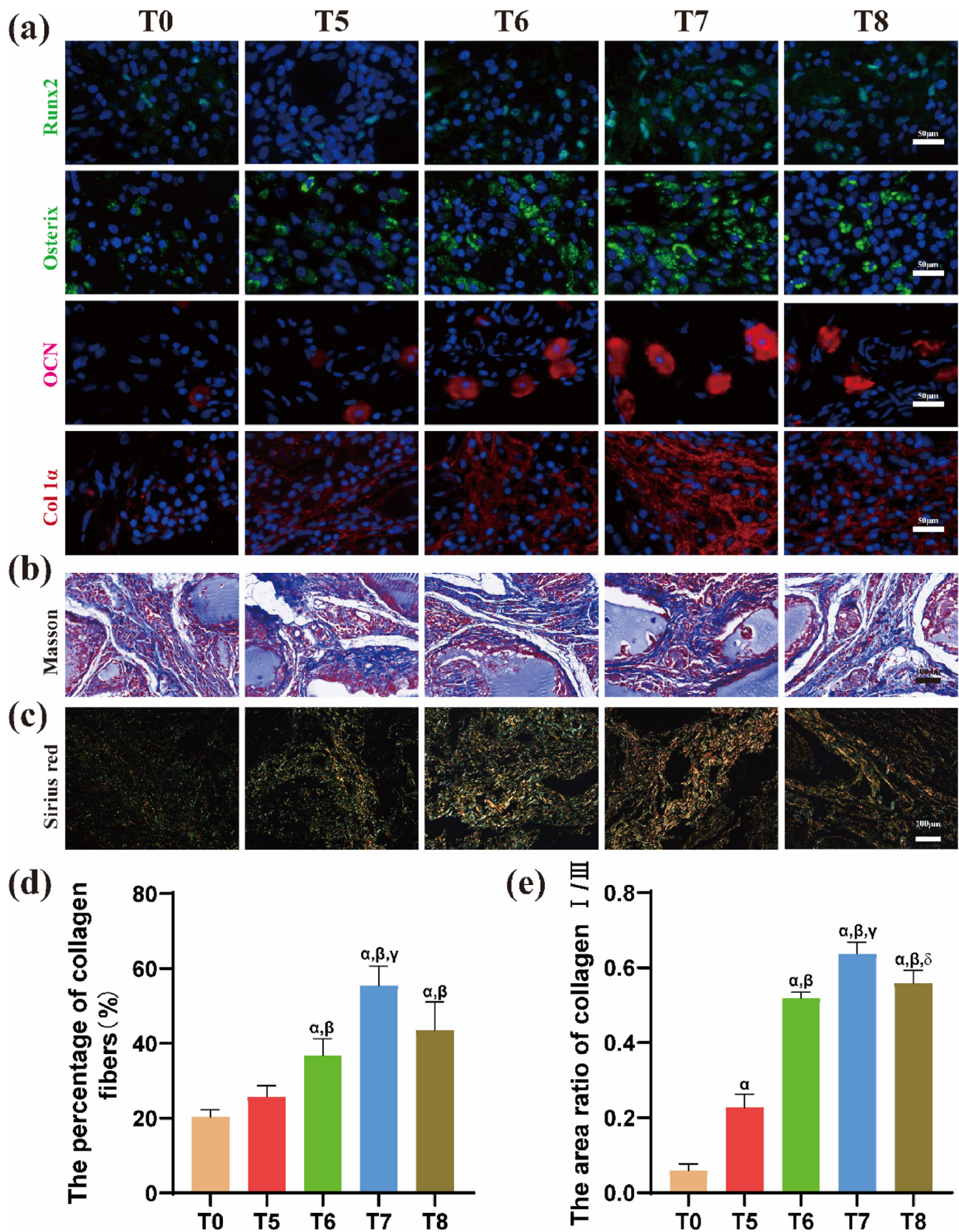
Fig. 5. Osteogenic differentiation after ectopic implantation of hydrogel scaffolds with different densities of BMSCs for 4 weeks. (a) Immunofluorescence staining images of osteogenic related proteins Runx2 (green), Osterix (green), OCN (red), and Col-1a (red). Cell nuclei stained in blue. Scale bar: 50 μm. (b) Masson staining of isolated tissues showing collagen deposition (blue), and (c) Collagen type I and III (orange-yellow indicates type I collagen, blue-green indicates type III collagen) as observed after Sirius red staining. Scale bar: 100 μm. (d) Quantitative results of the area of collagen and (e) the ratio of type I/III collagen. $^{\alpha}p<0.05$ vs T0; $^{\beta}p<0.05$ vs T5; $^{\gamma}p<0.05$ vs T6; $^{\delta}p<0.05$ vs T7. (For interpretation of the references to colour in this figure legend, the reader is referred to the Web version of this article.)

3.3.4. Masson and sirius red staining

Collagen fibers appeared blue under Masson staining and exhibited a cord-like structure (Fig. 5b). The samples were stained with Sirius red and observed under a polarized light microscope to determine the types of collagen fibers. Type I collagen showed an orange-yellow color, whereas type III collagen showed a blue-green color (Fig. 5c). The amount of collagen produced and the ratio of type I to type III collagen were evaluated and quantitatively compared using ImageJ software. Staining results (Fig. 5d) showed that the percentage of collagen fibers in T7 group ($55.47 \pm 5.21\%$) was significantly higher relative to that of T6 ($36.67 \pm 4.57\%$) and T8 ($43.53 \pm 7.48\%$) groups ($p < 0.05$). The ratio of type I/III was highest in the T7 group (0.64 ± 0.03), and no significant difference in the ratio of type I and type III was observed between the T6 (0.52 ± 0.01) and T8 (0.56 ± 0.03) groups (Fig. 5e).

3.4. Signaling pathway analysis

3.4.1. Gene expression and bioinformatic analyses

Based on the results of the above experiments. A cell density of 1×10^7/mL (Hyd_Lap group) was used to explore the potential mechanism

by which laponite promotes bone formation. Bioprinted hydrogels without laponite loaded with the same density of BMSCs were used as controls (Hyd group). The genes identified and expressed in the 2nd week after printing are shown in Fig. 6a. A total of 2, 068 up-regulated and 2, 491 down-regulated genes were identified in the Hyd_Lap group compared to those in the Hyd group. Gene Ontology (GO) analysis of differentially expressed genes showed that ossification-related genes, such as Bmp2, Col1a, and Sp7, were upregulated in Hyd_Lap (Fig. 6b), consistent with previous results from osteogenesis experiments. KEGG pathway analysis was performed to investigate the potential mechanisms. The top 20 enriched pathways are presented in Fig. 6c, with the PI3K/AKT pathway being the most significantly enriched pathway.

3.4.2. Protein quantitation analyses of key markers in the PI3K/AKT pathway

Western blotting was performed to determine the expression levels of various marker proteins (PI3K, AKT, and mTOR) in the PI3K/AKT pathway and to test their phosphorylation in the blank, Hyd, and Hyd_Lap groups to verify PI3K/AKT pathway activation. Western blot results and protein quantitative analysis showed that the
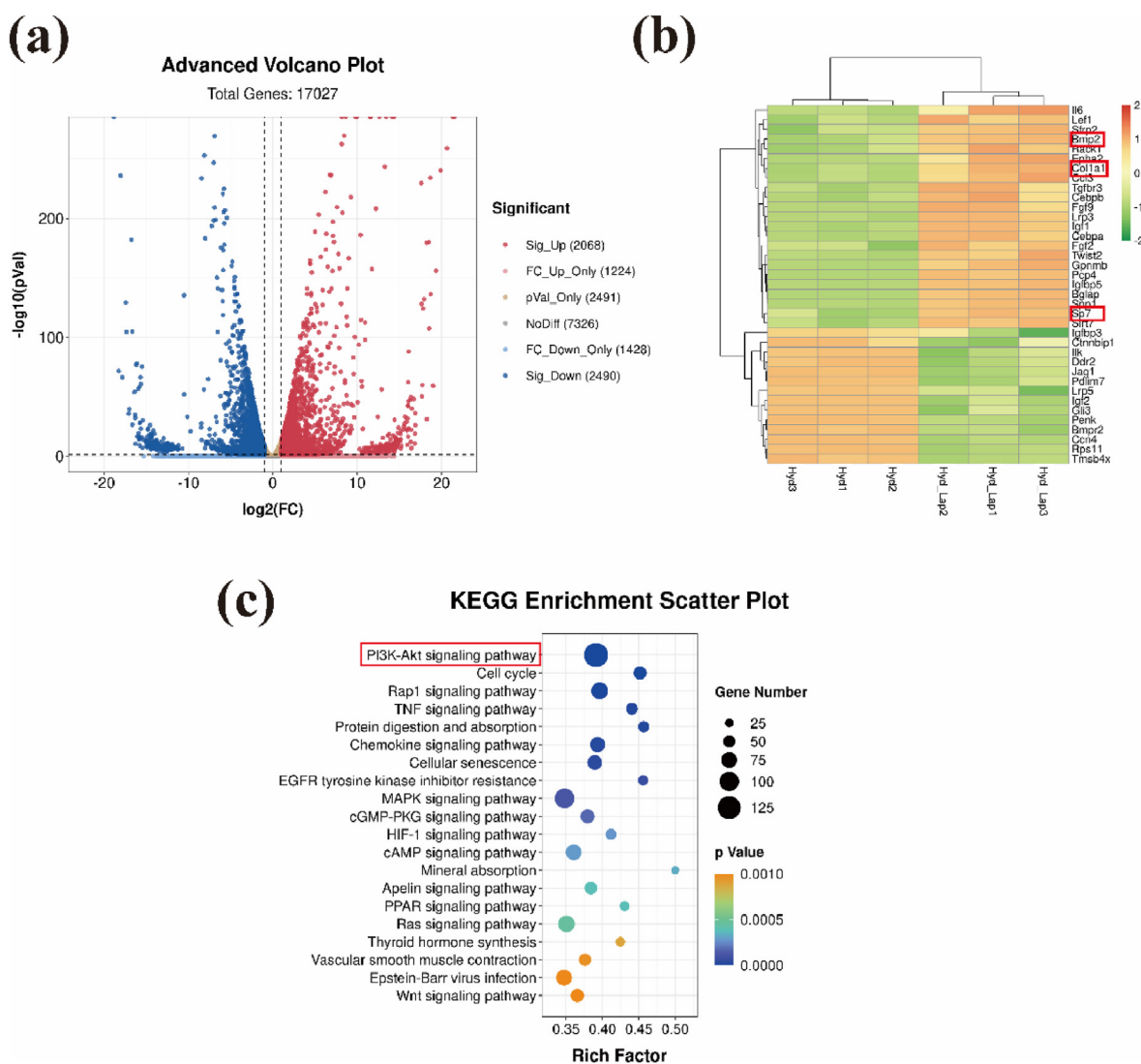

Fig. 6. Gene expression and analysis of biological activity of BMSCs cultured in Hyd_Lap and Hyd groups. (a) Volcano plots showing mRNA expression profiles of BMSCs cultured in the two groups (red represents upregulated genes, blue represents downregulated genes). (b) Heat map showing expression levels of osteogenesis-associated genes identified by GO enrichment analysis. (c) KEGG pathway gene enrichment analysis. The PI3K/AKT pathway, highlighted with a red box, was highly enriched. (For interpretation of the references to colour in this figure legend, the reader is referred to the Web version of this article.)

phosphorylation levels of the three proteins (PI3K, AKT, and mTOR) in BMSCs cultured in the Hyd_Lap group were significantly higher than those in the Hyd and blank groups (Fig. 7a and Fig. 7b, p < 0.05).

LY294002, an inhibitor of PI3K, was added to the Hyd_Lap group to block PI3K/AKT pathway activation and to verify that laponite promotes the osteogenic differentiation of BMSCs through this pathway. The expression levels of osteogenesis-related proteins Runx2 and Col1a and mineralization in the bioprinted hydrogels were evaluated. The expression levels of key osteogenic proteins (Runx2 and Col-1a) were upregulated in the Hyd_Lap group compared with those in the Hyd group, whereas the expression of these proteins was significantly downregulated after LY294002 treatment (Fig. 7c and d). Alizarin Red S staining showed consistent results; the area of mineralized nodules in the Hyd_Lap group was larger than that in the Hyd and Hyd_Lap + LY294002 groups (Fig. 7e and f).

3.5. Bone defects repair experiment

The amount of new bone formed in Hyd_Lap group on week 8 was significantly higher relative to the amount of bone formed in the other groups. The amount of new bone formed in the Hyd_Lap + LY294002 group was not significantly different from that in the blank group, as shown by the micro-CT scan and 3D reconstruction analysis (Fig. 8a). The volume ratios of new bone to total tissue (BV/TV) showed a higher volume of new bone in the defect area in the Hyd_Lap group than in the Hyd group (p < 0.05; Fig. 8b). However, low amount of newly formed bone was observed in the Hyd_Lap + LY294002 group compared with the amount of bone formed in the Hyd_Lap group. In addition, the TbTh and TbN levels in the Hyd_Lap group were higher than those in the other groups (p < 0.05; Fig. 8c and d). In addition, the amount of new bone formed in the Hyd_Lap (no BMSCs) group was significantly lower than that in the Hyd_Lap group (Fig. 8a–d), indicating that BMSCs are essential for bone regeneration in the hydrogels.

Van Gieson staining showed higher new bone formation at the edge of the defect area in the Hyd_Lap group relative to the amount of bone formed in the Hyd and Hyd_Lap + LY294002 groups. In contrast, the blank group exhibited only partial fibrous tissue formation (Fig. 8e).

To confirm the effect of implanted hydrogel materials and the inhibitor LY294002 on rats for a long period, the rat heart, liver, spleen, lung, and kidney were sectioned and subjected to H&E staining after implantation for 8 weeks. No abnormal histopathological morphology was observed in the visceral tissues (Fig. S4), indicating that neither the hydrogel material nor the inhibitor caused any systemic toxicity or damage.

4. Discussion

The efficacy of printed constructs is associated with different factors determined by their bioinks, including biocompatibility, biodegradability, bioprintability, and mechanical integrity [2]. The incorporation of nanomaterials into hydrogels improves the mechanical strength of polymer networks; thus, composite hydrogels exhibit excellent mechanical properties with superior biological properties [20]. Laponite plays an important role in three-dimensional (3D) printing. The application of laponite in 3D printing has been attributed to its unique properties. Laponite can be used to enhance the mechanical capacity of hydrogels when incorporated into bioinks [12,21]. In addition, laponite can strengthen cell adhesion in hydrogels [1] and promote the transformation of cells toward osteoblastic differentiation [11].

The broad diffraction peak of gelatin at 12°–33° can reflect moderate crystallinity (Fig. 1c). In the biocomposite, the representative peak of alginate at 2 theta 13° was missing, which might be due to the cross-linking of alginate with calcium ions that formed a more regular structure [22]. In addition, the diffraction peaks at 2 theta 35° and 61° in the biocomposite were reduced relative to those of laponite, which might have been caused by the charge absorption of laponite [23]. Thus, the

biocomposite formed a stable regular structure. A relatively broad absorption peak was observed near 3452 cm^{-1} in the infrared spectrum of laponite and the biocomposite (Fig. 1d) due to the –OH stretching vibration and the peak of hydroxyl hydrogen bonds between crystal layers. It also exhibited a bending vibration absorption peak of the adsorbed water molecule –OH at 1640 cm^{-1} and a stretching vibration absorption peak of the Si–O bond in the lattice at 1013 cm^{-1}. The characteristic absorption peaks of laponite appeared in the composite, indicating that laponite still existed in the layered crystal structure of the composite after bioprinting, and functioned in the form of nanosheets.

Shear-thinning hydrogels, such as gelatin and alginate, have many advantages in 3D bioprinting compared to other biomaterials. Owing to their rheological properties, such as the Herschel-Bulkley flow and stress-relaxation behaviors, making hydrogel materials injectable through a needle [10]. The main limitations of these hydrogels for bone repair are their low structural reliability and precision. Moreover, the bio-ink used for 3D printing is highly hydrophilic with a high swelling rate, which can cause deformation of the printed structure, significant reduction in resolution, and mechanical hysteresis [24,25]. For example, structures with an elastic and conductive 3D printed ionic composite hydrogel easily deform owing to their high swelling ratios of up to 3500% [26]. In contrast, the swelling ratio of the BMSC-laponite hydrogel in the present study was less than 1100%, which was attributed to the introduction of laponite.

The addition of laponite to the hydrogels significantly improved their mechanical properties, including tensile strength, elasticity modulus, and dynamic behaviors (such as viscoelasticity) [10,27]. The findings of a previous study showed that the compressive modulus of hydrogels containing 2% laponite (101.41 ± 3.11 kPa) exhibited approximately 2.2-fold increase compared with that of hydrogels without laponite (46.98 ± 1.54 kPa) [12]. Composite hydrogels can be molded into free-standing objects with persistent shapes owing to their extremely high mechanical strength at room temperature (24 °C) and the strong electrostatic interactions of laponite [28]. The hydrogels may become milder for laden cells to smoothly pass through the printing needle at higher temperatures (30 °C).

The mechanical strength of 3D hydrogel constructs plays an important role in maintaining stereoscopic structures and regulating cellular activities. However, studies have not explored whether the density of laden cells can inhibit the cross-linking of molecules and decrease their mechanical properties. The mechanical strength of the hydrogel constructs with the highest cell density (10^8/mL) was significantly lower than that of hydrogels with lower or no cell densities. The mechanical strength of the composite hydrogel was mainly maintained by the internal laponite and sodium alginate cross-linked with calcium ions. The diameter of cells is about 15 μm [29], so the average distance between cells at a density of 10^8/mL is less than 20 μm, and the distance will be smaller as the cells proliferate. Excessive cell density and the small distance between cells inside the hydrogel may inhibit the cross-linking and the electrostatic adsorption partly, thus reducing the overall mechanical strength. The reduction in cell density (below 10^7/mL) provided sufficient space for the cross-linking; therefore, the mechanical strength of the hydrogel structures did not decrease significantly.

The addition of laponite increased the structural stability and mechanical properties of the hydrogel constructs, and enhanced the adhesion, spreading, and proliferation of cells inside the hydrogels [24]. Experiments using mouse pre-osteoblast cells showed good adhesion, spreading, and proliferation effects attributed to the formation of a laponite composite [30], which is consistent with the results of the present study. Some effects were attributed to differences in cell density. Cells at all the investigated densities exhibited higher proliferative activity in the 3D hydrogel construct on day 14 of culture. The proliferation rates in the T5 and T6 groups were significantly lower than those in the T7 and T8 groups were. Notably, the number of dead cells gradually increased with the number of live cells. The number of viable cells in T8 was less than 90% on day 3 and less than 85% on day 14, whereas the
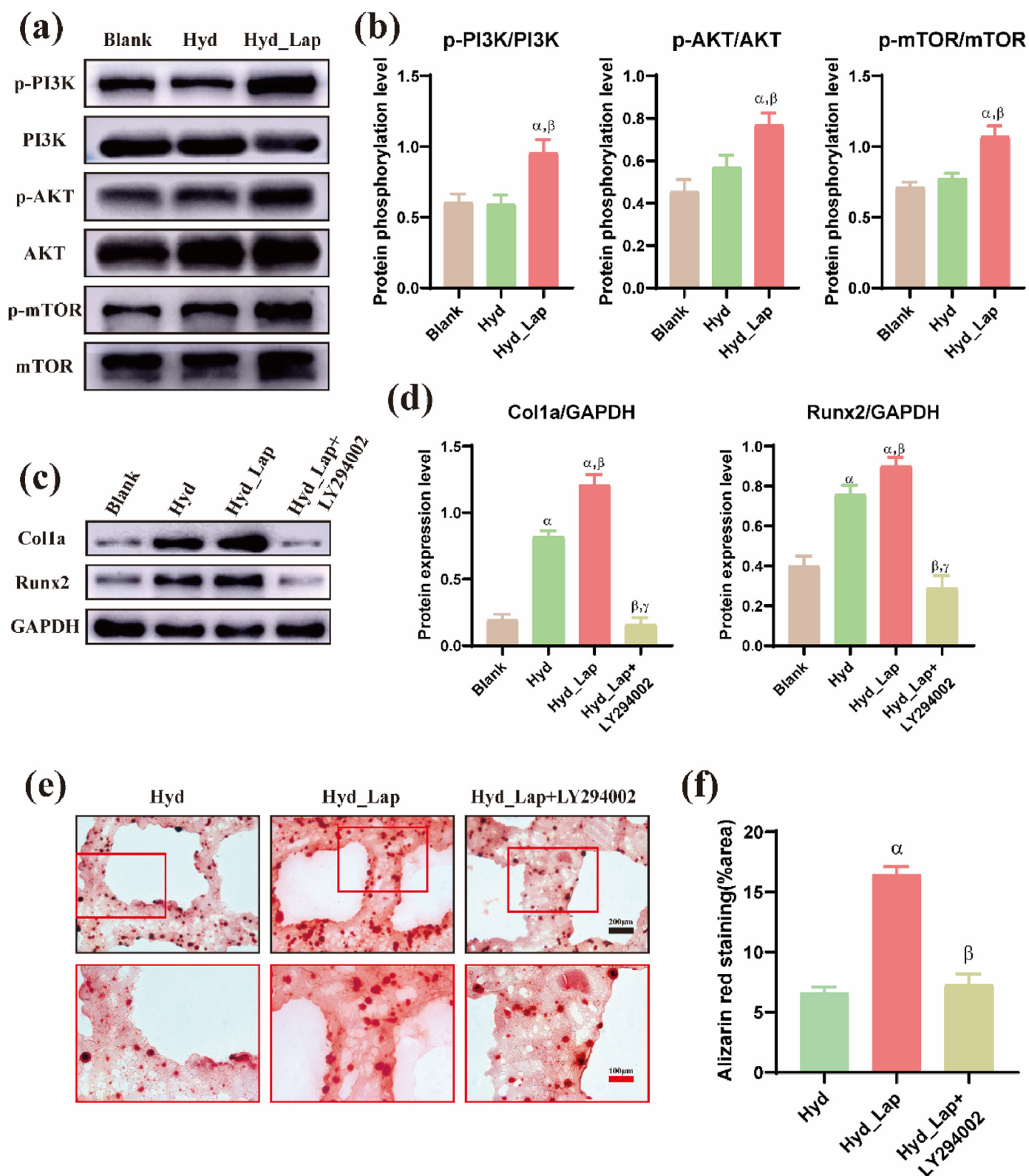
Fig. 7. Laponite activates PI3K/AKT signal transduction pathway-related proteins (p-PI3K, *p*-AKT) of BMSCs in hydrogel scaffolds to promote osteogenic differentiation *in vitro*. Expression levels of target proteins as determined by western blotting (a) and phosphorylation levels of PI3K, AKT and mTOR proteins were significantly higher in Hyd_Lap group (b) compared with Blank and Hyd groups. [α]p<0.05 vs Blank; [β]p<0.05 vs Hyd. (c, d) Expression levels of Runx2 and Col 1α in Hyd_Lap group, Blank and Hyd groups. Protein levels of Runx2 and Col 1α were significantly suppressed in Hyd_Lap + LY294002 group after treatment with LY294002. [α]p<0.05 vs Blank; [β]p<0.05 vs Hyd; [γ]p<0.05 vs Hyd_Lap. (e, f) Mineralization nodules were higher in Hyd_Lap than in Hyd group, and treatment of LY294002 reduced mineralization nodules. Scale bars: black 200 μm; red 100 μm [α]p<0.05 vs Hyd; [β]p<0.05 vs Hyd_Lap. (For interpretation of the references to colour in this figure legend, the reader is referred to the Web version of this article.)
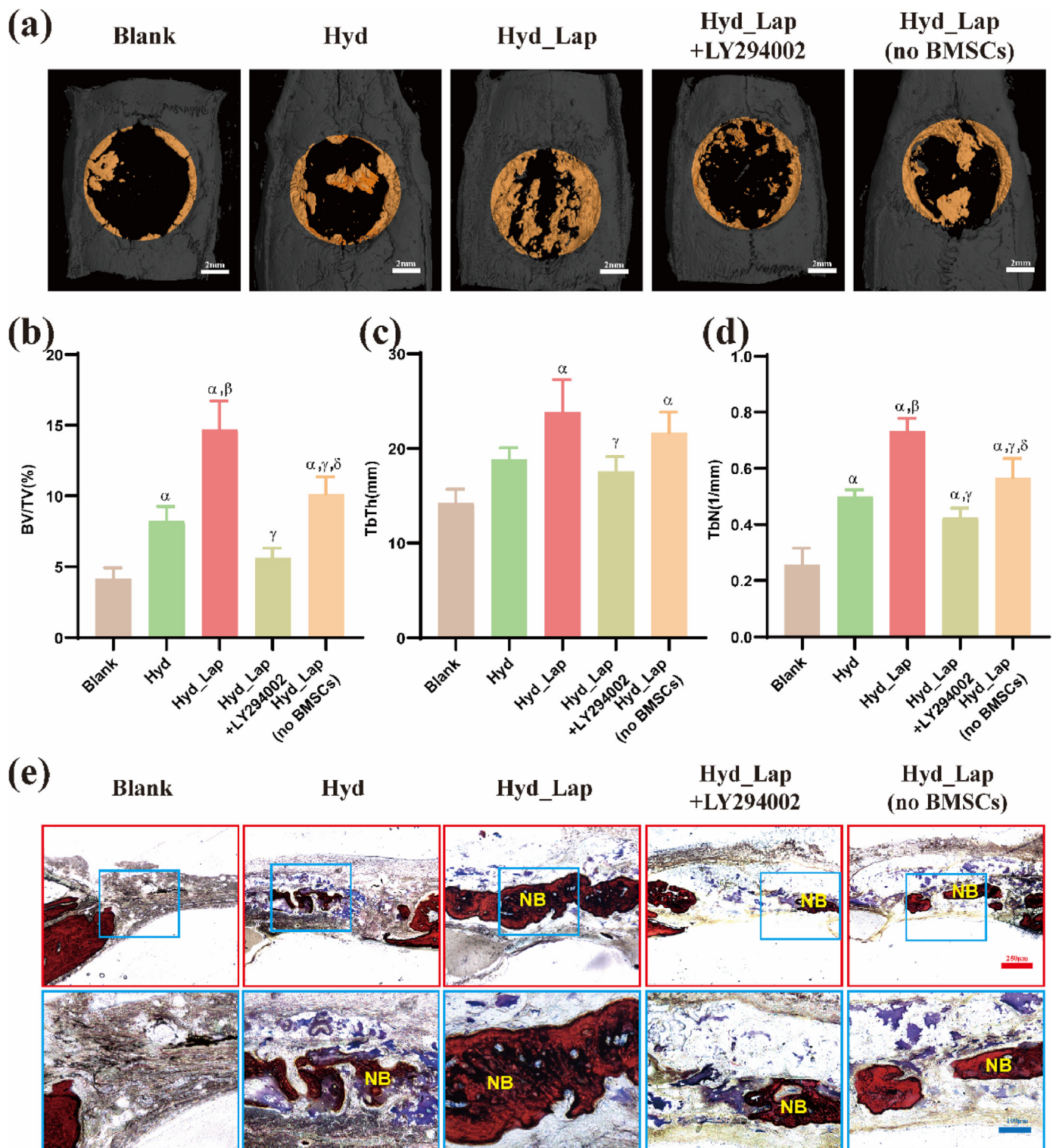
Fig. 8. Bone repair effects of biological hydrogel scaffolds containing laponite using cranial defect rat models 8 weeks after implantation as determined by Micro-CT analysis and Van Gieson staining. (a) Micro-CT 3D reconstruction of new bone formation (yellow color indicates new bone). (b) New bone volume/tissue volume (BV/TV) ratio, (c) Trabecular bone thickness (TbTh) and (d) the number of trabecular bone (TbN) of the skull defect area in each group. $^{\alpha}p<0.05$ vs Blank; $^{\beta}p<0.05$ vs Hyd; $^{\gamma}p<0.05$ vs Hyd_Lap. (e) Histological analysis of tissues by VG staining. NB: new bone. (For interpretation of the references to colour in this figure legend, the reader is referred to the Web version of this article.)

survival rates of the other three groups were >90% over 14 days. As we know, in the process of culture, as the cells proliferate, the number of cells increases, and the gap between them decreases. Both the supply of nutrients and discharge of metabolic waste are hindered, which affects

cell survival [31]. By the 14th day of culture, the corresponding limiting factors were more obvious and the number of dead cells increased, resulting in a lower survival rate. This indicates that this 3D hydrogel construct cannot provide sufficient oxygen and nutrients for cells at high

densities, and 10^7/mL was the optimal cell density for bioprinting.

Gaharwar et al. reported that laponite can promote *in vitro* osteogenic differentiation of human mesenchymal stem cells (hMSCs) without the addition of osteoinductive factors such as bone morphogenetic proteins-2 (BMP-2) or dexamethasone [11]. Okesola et al. integrated hyaluronic acid, peptide amphiphiles, and laponite into a bioactive hydrogel, and their findings showed that the composite stimulated osteoblastic differentiation without the addition of exogenous growth factors [32]. A set of events followed the classical temporal pattern of osteogenic differentiation, including marker-enhanced ALP activity, Runx2 transcript upregulation, bone-related matrix protein deposition (osteocalcin and osteopontin), and matrix mineralization [24]. Although previous results from *in vitro* studies indicated that laponite promotes osteogenic differentiation in a dose-dependent manner [33], laponite-induced ectopic osteogenesis has not been fully evaluated. In the current study, 3D bioprinted laponite hydrogel constructs with different BMSC densities were implanted into an SD rat posterior gluteal muscle pouch model and their ectopic osteogenic abilities were explored. The Laponite hydrogel alone did not promote bone formation and was infiltrated by fibrous tissue, an expected result in the rat ectopic muscle pouch model [34]. On the contrary, the addition of BMSCs to the scaffold induced ectopic bone formation, as shown by X-ray, EDS analysis, micro-CT examination, and histomorphological analysis. Therefore, mineralization and bone formation in this composite hydrogel are associated with the presence of BMSCs. A higher type I/III collagen ratio, as well as regular patterns of collagen in the bone layers, were observed by Sirius red staining. Type I collagen is the major protein component of the bone extracellular matrix, and collagen fiber orientation majorly contributes to the maturation and strength of newly formed bone tissues [35].

The density of cell-composite biomaterials is vital for bone-tissue engineering. Therefore, it is important to explore the effect of the BMSC density in hydrogel scaffolds containing laponite on osteogenic differentiation. The high cell density (in the T5, T6, and T7 groups) in the bioprinted constructs was associated with the stronger bone-promoting effect of laponite. However, the bone-promoting effects decreased when the cell density reached 10^8/mL, which can be attributed to the ratio of cells to laponite [36]. The same amount of Laponite was used in all composites, as identical volumes of the hydrogel construct were used. The amount of laponite degradation products taken up by a single cell decreased with increasing cell density, thus reducing the osteogenic effect.

The degradation products of laponite, such as Mg^+, Li^+, and silicic acid, can induce osteogenic differentiation of mesenchymal stem cells and promote bone formation by stimulating the Wnt/β-catenin signaling pathway [13]. Thus, in our study, the osteogenic function of laponite may be mostly attributed to the synergistic effect of various ions. The differences in the expression of BMSC genes in the hydrogel constructs under the action of laponite were explored using transcriptomic analysis. These findings showed that the differentially expressed genes were mainly enriched in the PI3K/AKT pathway. Previous studies have reported that activation of the PI3K/AKT signaling pathway promotes bone formation [37].

PI3K/AKT is involved in the regulation of several cellular processes including cell division, autophagy, survival, and differentiation. More than 150 proteins have been identified as mediators of PI3K/AKT pathway [38,39]. PI3K/AKT/mTOR signaling pathway is essential for normal metabolism in joint tissues and is involved in bone degeneration [40]. Lin et al. reported that the PI3K/AKT pathway is activated during subchondral ossification in osteoarthritis, and ossification is significantly suppressed after treatment with an inhibitor of this pathway [41]. Moreover, our findings showed that the activation of PI3K/AKT promotes bone formation.

The role of the PI3K/AKT pathway in regulating bone formation was explored *in vivo* and *in vitro*. As shown in the results, bone formation was reduced after pathway inhibition, which could be used as a new strategy to promote the osteogenesis of biomaterials. However, the PI3K inhibitor did not completely abrogate the osteogenic effects of laponite, implying that the osteogenic effect of laponite is not entirely attributed to the modulation of the PI3K/AKT pathway. Other signaling pathways, such as Wnt/β-catenin, also play important roles [13].

Although it has been confirmed that the laponite hydrogel can promote osteogenic differentiation of BMSCs through the PI3K/AKT pathway as well as enhance extracellular matrix formation and mineralization, the specific target has not been fully elucidated. Further studies should conduct in-depth investigations of the specific mechanisms to establish interconnections between pathways.

5. Conclusion

This study presents a new strategy for the development of a 3D printed laponite bioink loaded with BMSCs to induce bone regeneration. The related osteogenesis mechanisms were comprehensively explored. The bioink protected the encapsulated cells from shear stress during bioprinting and promoted cell growth and cell spreading. Furthermore, the 3D bioprinted construct promoted the transformation of BMSCs towards osteoblastic differentiation and induced ectopic bone formation without the addition of exogenous bone growth factors. BMSCs at a density of 10^7/mL in the bio-printed construct exhibited the highest osteogenic ability. The inherent osteogenic properties of the laponite hydrogel were exhibited through the activation of the PI3K/AKT signaling pathway and suppressed by a PI3K inhibitor. The 3D bioprinted construct effectively repaired bone defects by delivering BMSCs, as shown in the rat model, verifying the *in vivo* role of the PI3K/AKT signaling pathway. These findings indicate that the 3D bioprinted laponite hydrogel construct can be used as a substitute for conventional grafting in the reconstruction of bone defects.

Credit author statement

Sheng Miao: Conceptualization, Methodology, Writing, Data curation, Writing – original draft preparation. Jinru Zhou: Investigation, Methodology, Formal analysis. Bin Liu: Methodology, Formal analysis. Xing Lei: Formal analysis, Software. Taoran Wang: Visualization. Xiaotian Hao: Data curation. Pengzhen Cheng: Visualization. Hao Wu and Yue Song: Investigation. Guoxian Pei: Methodology, Resources, Supervision, Validation, Funding acquisition. Long Bi: Project administration, Writing – review & editing, Funding acquisition.

Data availability

The data sets used and/or analyzed during the current study area-vailable from the corresponding author on reasonable request.

Declaration of competing interest

The authors declare that they have no known competing financial interests or personal relationships that could have appeared to influence the work reported in this paper.

Appendix A. Supplementary data

Supplementary data to this article can be found online at https://doi.org/10.1016/j.mtbio.2022.100342.

References

[1] P. Baldwin, D.J. Li, D.A. Auston, H.S. Mir, R.S. Yoon, K.J. Koval, Autograft, allograft, and bone graft substitutes: clinical evidence and indications for use in the setting of orthopaedic trauma surgery, J. Orthop. Trauma 33 (4) (2019) 203, https://doi.org/10.1097/BOT.0000000000001420.

[2] G. Decante, J.B. Costa, J. Silva-Correia, M.N. Collins, R.L. Reis, J.M. Oliveira, Engineering bioinks for 3D bioprinting, Biofabrication 13 (3) (2021), https://doi.org/10.1088/1758-5090/abec2c.

[3] Y. Chen, Y. Chen, X. Xiong, R. Cui, G. Zhang, C. Wang, D. Xiao, S. Qu, J. Weng, Hybridizing gellan/alginate and thixotropic magnesium phosphate-based hydrogel scaffolds for enhanced osteochondral repair, Mater Today Bio 14 (2022), 100261, https://doi.org/10.1016/j.mtbio.2022.100261.

[4] M.A. Heinrich, W. Liu, A. Jimenez, J. Yang, A. Akpek, X. Liu, Q. Pi, X. Mu, N. Hu, R.M. Schiffelers, J. Prakash, J. Xie, Y.S. Zhang, 3D bioprinting: from benches to translational applications, Small 15 (23) (2019), e1805510, https://doi.org/10.1002/smll.201805510.

[5] W. Sun, B. Starly, A.C. Daly, J.A. Burdick, J. Groll, G. Skeldon, W. Shu, Y. Sakai, M. Shinohara, M. Nishikawa, J. Jang, D.W. Cho, M. Nie, S. Takeuchi, S. Ostrovidov, A. Khademhosseini, R.D. Kamm, V. Mironov, L. Moroni, I.T. Ozbolat, The bioprinting roadmap, Biofabrication 12 (2) (2020), 022002, https://doi.org/10.1088/1758-5090/ab5158.

[6] J.M. Sobral, S.G. Caridade, R.A. Sousa, J.F. Mano, R.L. Reis, Three-dimensional plotted scaffolds with controlled pore size gradients: effect of scaffold geometry on mechanical performance and cell seeding efficiency, Acta Biomater. 7 (3) (2011) 1009, https://doi.org/10.1016/j.actbio.2010.11.003.

[7] F. Iberite, E. Gruppioni, L. Ricotti, Skeletal muscle differentiation of human iPSCs meets bioengineering strategies: perspectives and challenges, NPJ Regen Med. 7 (1) (2022) 23, https://doi.org/10.1038/s41536-022-00216-9.

[8] S. Murugesan, T. Scheibel, Copolymer/clay nanocomposites for biomedical applications, Adv. Funct. Mater. 30 (17) (2020), https://doi.org/10.1002/adfm.201908101.

[9] B. Liu, Y. Bian, S. Liang, M. Yuan, S. Dong, F. He, S. Gai, P. Yang, Z. Cheng, J. Lin, One-step integration of tumor microenvironment-responsive calcium and copper peroxides nanocomposite for enhanced chemodynamic/ion-interference therapy, ACS Nano 16 (2021) 617, https://doi.org/10.1021/acsnano.1c07893.

[10] S. Afewerki, L. Magalhaes, A.D.R. Silva, T.D. Stocco, E.C. Silva Filho, F.R. Marciano, A.O. Lobo, Bioprinting a synthetic smectic clay for orthopedic applications, Adv Healthc Mater 8 (13) (2019), e1900158, https://doi.org/10.1002/adhm.201900158.

[11] A.K. Gaharwar, S.M. Mihaila, A. Swami, A. Patel, S. Sant, R.L. Reis, A.P. Marques, M.E. Gomes, A. Khademhosseini, Bioactive silicate nanoplatelets for osteogenic differentiation of human mesenchymal stem cells, Adv. Mater. 25 (24) (2013) 3329, https://doi.org/10.1002/adma.201300584.

[12] B. Liu, J. Li, X. Lei, P. Cheng, Y. Song, Y. Gao, J. Hu, C. Wang, S. Zhang, D. Li, H. Wu, H. Sang, L. Bi, G. Pei, 3D-bioprinted functional and biomimetic hydrogel scaffolds incorporated with nanosilicates to promote bone healing in rat calvarial defect model, Mater. Sci. Eng. C Mater. Biol. Appl. 112 (2020), 110905, https://doi.org/10.1016/j.msec.2020.110905.

[13] X. Zhang, J. Fan, C.S. Lee, S. Kim, C. Chen, M. Lee, Supramolecular hydrogels based on nanoclay and guanidine-rich chitosan: injectable and moldable osteoinductive carriers, ACS Appl. Mater. Interfaces 12 (14) (2020), 16088, https://doi.org/10.1021/acsami.0c01241.

[14] Y. Zhou, X. Xin, L. Wang, B. Wang, L. Chen, O. Liu, D.W. Rowe, M. Xu, Senolytics improve bone forming potential of bone marrow mesenchymal stem cells from aged mice, NPJ Regen Med. 6 (1) (2021) 34, https://doi.org/10.1038/s41536-021-0145-z.

[15] M. Pavel, M. Renna, S.J. Park, F.M. Menzies, T. Ricketts, J. Fullgrabe, A. Ashkenazi, R.A. Frake, A.C. Lombarte, C.F. Bento, K. Franze, D.C. Rubinsztein, Contact inhibition controls cell survival and proliferation via YAP/TAZ-autophagy axis, Nat. Commun. 9 (1) (2018) 2961, https://doi.org/10.1038/s41467-018-05388-x.

[16] J.M. Ayuso, S. Rehman, M. Farooqui, M. Virumbrales-Munoz, V. Setaluri, M.C. Skala, D.J. Beebe, Microfluidic tumor-on-a-chip model to study tumor metabolic vulnerability, Int. J. Mol. Sci. 21 (23) (2020), https://doi.org/10.3390/ijms21239075.

[17] J. Fang, X. Zhao, S. Li, X. Xing, H. Wang, P. Lazarovici, W. Zheng, Protective mechanism of artemisinin on rat bone marrow-derived mesenchymal stem cells against apoptosis induced by hydrogen peroxide via activation of c-Raf-Erk1/2-p90(rsk)-CREB pathway, Stem Cell Res. Ther. 10 (1) (2019) 312, https://doi.org/10.1186/s13287-019-1419-2.

[18] A. Sheikhi, S. Afewerki, R. Oklu, A.K. Gaharwar, A. Khademhosseini, Effect of ionic strength on shear-thinning nanoclay-polymer composite hydrogels, Biomater. Sci. 6 (8) (2018) 2073, https://doi.org/10.1039/c8bm00469b.

[19] C. Boyer, L. Figueiredo, R. Pace, J. Lesoeur, T. Rouillon, C.L. Visage, J.F. Tassin, P. Weiss, J. Guicheux, G. Rethore, Laponite nanoparticle-associated silated hydroxypropylmethyl cellulose as an injectable reinforced interpenetrating network hydrogel for cartilage tissue engineering, Acta Biomater. 65 (2018) 112, https://doi.org/10.1016/j.actbio.2017.11.027.

[20] Z. Wang, J. Zhao, W. Tang, L. Hu, X. Chen, Y. Su, C. Zou, J. Wang, W.W. Lu, W. Zhen, R. Zhang, D. Yang, S. Peng, Multifunctional nanoengineered hydrogels consisting of black phosphorus nanosheets upregulate Bone Formation, Small 15 (41) (2019), e1901560, https://doi.org/10.1002/smll.201901560.

[21] C. Le Coeur, C. Lorthioir, A. Feoktystov, B. Wu, G. Volet, C. Amiel, Laponite/poly(2-methyl-2-oxazoline) hydrogels: interplay between local structure and rheological behaviour, J. Colloid Interface Sci. 582 (Pt A) (2021) 149, https://doi.org/10.1016/j.jcis.2020.07.068.

[22] M. Roozbahani, M. Kharaziha, R. Emadi, pH sensitive dexamethasone encapsulated laponite nanoplatelets: release mechanism and cytotoxicity, Int. J. Pharm. 518 (1–2) (2017) 312, https://doi.org/10.1016/j.ijpharm.2017.01.001.

[23] A.S. Vaziri, I. Alemzadeh, M. Vossoughi, A.C. Khorasani, Co-microencapsulation of Lactobacillus plantarum and DHA fatty acid in alginate-pectin-gelatin biocomposites, Carbohydr. Polym. 199 (2018) 266, https://doi.org/10.1016/j.carbpol.2018.07.002.

[24] A.R. Spencer, E. Shirzaei Sani, J.R. Soucy, C.C. Corbet, A. Primbetova, R.A. Koppes, N. Annabi, Bioprinting of a cell-laden conductive hydrogel composite, ACS Appl. Mater. Interfaces 11 (34) (2019), 30518, https://doi.org/10.1021/acsami.9b07353.

[25] Y. Zhang, J. Li, V.H.M. Mouser, N. Roumans, L. Moroni, P. Habibovic, Biomimetic mechanically strong one-dimensional hydroxyapatite/poly(d,l-lactide) composite inducing formation of anisotropic collagen matrix, ACS Nano 15 (2021), 17480, https://doi.org/10.1021/acsnano.1c03905.

[26] J. Odent, T.J. Wallin, W. Pan, K. Kruemplestaedter, R.F. Shepherd, E.P. Giannelis, Highly elastic, transparent, and conductive 3D-printed ionic composite hydrogels, Adv. Funct. Mater. 27 (33) (2017), https://doi.org/10.1002/adfm.201701807.

[27] P. Shi, Y.H. Kim, M. Mousa, R.R. Sanchez, R.O.C. Oreffo, J.I. Dawson, Self-assembling nanoclay diffusion gels for bioactive osteogenic microenvironments, Adv Healthc Mater 7 (15) (2018), e1800331, https://doi.org/10.1002/adhm.201800331.

[28] R.K. Avery, H. Albadawi, M. Akbari, Y.S. Zhang, M.J. Duggan, D.V. Sahani, B.D. Olsen, A. Khademhosseini, R. Oklu, An injectable shear-thinning biomaterial for endovascular embolization, Sci. Transl. Med. 8 (365) (2016), https://doi.org/10.1126/scitranslmed.aah5533, 365ra156.

[29] H.H. Lipowsky, D.T. Bowers, B.L. Banik, J.L. Brown, Mesenchymal stem cell deformability and implications for microvascular sequestration, Ann. Biomed. Eng. 46 (4) (2018) 640, https://doi.org/10.1007/s10439-018-1985-y.

[30] A.K. Gaharwar, P.J. Schexnailder, B.P. Kline, G. Schmidt, Assessment of using laponite cross-linked poly(ethylene oxide) for controlled cell adhesion and mineralization, Acta Biomater. 7 (2) (2011) 568, https://doi.org/10.1016/j.actbio.2010.09.015.

[31] M.A. Skylar-Scott, S.G.M. Uzel, L.L. Nam, J.H. Ahrens, R.L. Truby, S. Damaraju, J.A. Lewis, Biomanufacturing of organ-specific tissues with high cellular density and embedded vascular channels, Sci. Adv. 5 (9) (2019), eaaw2459, https://doi.org/10.1126/sciadv.aaw2459.

[32] B.O. Okesola, S. Ni, B. Derkus, C.C. Galeano, A. Hasan, Y. Wu, J. Ramis, L. Buttery, J.I. Dawson, M. D'Este, R.O.C. Oreffo, D. Eglin, H. Sun, A. Mata, Growth-factor free multicomponent nanocomposite hydrogels that stimulate Bone Formation, Adv. Funct. Mater. 30 (14) (2020), https://doi.org/10.1002/adfm.201906205.

[33] S.M. Mihaila, A.K. Gaharwar, R.L. Reis, A. Khademhosseini, A.P. Marques, M.E. Gomes, The osteogenic differentiation of SSEA-4 sub-population of human adipose derived stem cells using silicate nanoplatelets, Biomaterials 35 (33) (2014) 9087, https://doi.org/10.1016/j.biomaterials.2014.07.052.

[34] D.B. Raina, D. Larsson, F. Mrkonjic, H. Isaksson, A. Kumar, L. Lidgren, M. Tagil, Gelatin- hydroxyapatite- calcium sulphate based biomaterial for long term sustained delivery of bone morphogenic protein-2 and zoledronic acid for increased bone formation: in-vitro and in-vivo carrier properties, J. Contr. Release 272 (2018) 83, https://doi.org/10.1016/j.jconrel.2018.01.006.

[35] M. Unal, A. Creecy, J.S. Nyman, The role of matrix composition in the mechanical behavior of bone, Curr. Osteoporos. Rep. 16 (3) (2018) 205, https://doi.org/10.1007/s11914-018-0433-0.

[36] A.K. Gaharwar, L.M. Cross, C.W. Peak, K. Gold, J.K. Carrow, A. Brokesh, K.A. Singh, 2D nanoclay for biomedical applications: regenerative medicine, therapeutic delivery, and additive manufacturing, Adv. Mater. 31 (23) (2019), e1900332, https://doi.org/10.1002/adma.201900332.

[37] C. Yang, X. Liu, K. Zhao, Y. Zhu, B. Hu, Y. Zhou, M. Wang, Y. Wu, C. Zhang, J. Xu, Y. Ning, D. Zou, miRNA-21 promotes osteogenesis via the PTEN/PI3K/Akt/HIF-1alpha pathway and enhances bone regeneration in critical size defects, Stem Cell Res. Ther. 10 (1) (2019) 65, https://doi.org/10.1186/s13287-019-1168-2.

[38] M. Jafari, E. Ghadami, T. Dadkhah, H. Akhavan-Niaki, PI3k/AKT signaling pathway: Erythropoiesis and beyond, J. Cell. Physiol. 234 (3) (2019) 2373, https://doi.org/10.1002/jcp.27262.

[39] F. Tang, Y. Wang, B.A. Hemmings, C. Ruegg, G. Xue, PKB/Akt-dependent regulation of inflammation in cancer, Semin. Cancer Biol. 48 (2018) 62, https://doi.org/10.1016/j.semcancer.2017.04.018.

[40] K. Sun, J. Luo, J. Guo, X. Yao, X. Jing, F. Guo, The PI3K/AKT/mTOR signaling pathway in osteoarthritis: a narrative review, Osteoarthritis Cartilage 28 (4) (2020) 400, https://doi.org/10.1016/j.joca.2020.02.027.

[41] C. Lin, Y. Shao, C. Zeng, C. Zhao, H. Fang, L. Wang, J. Pan, L. Liu, W. Qi, X. Feng, H. Qiu, H. Zhang, Y. Chen, H. Wang, D. Cai, C.J. Xian, Blocking PI3K/AKT signaling inhibits bone sclerosis in subchondral bone and attenuates post-traumatic osteoarthritis, J. Cell. Physiol. 233 (8) (2018) 6135, https://doi.org/10.1002/jcp.26460.